

## Laser-assisted atom probe tomography of Ti/TiN films deposited on Si<sup>‡</sup>

N. A. Sanford<sup>a,\*</sup>, P. T. Blanchard<sup>a</sup>, R. White<sup>b</sup>, M. R. Vissers<sup>c</sup>, D. R. Diercks<sup>d</sup>, A. V. Davydov<sup>e</sup>, and D. P. Pappas<sup>c</sup>

<sup>a</sup> National Institute of Standards and Technology, Physical Measurement Laboratory, Division 686, 325 Broadway, Boulder, CO 80305

<sup>b</sup> National Institute of Standards and Technology, Material Measurement Laboratory, Division 647, 325 Broadway, Boulder, CO 80305

<sup>c</sup> National Institute of Standards and Technology, Physical Measurement Laboratory, Division 687, 325 Broadway, Boulder, CO 80305

<sup>d</sup> Colorado School of Mines, Department of Metallurgical and Materials Engineering, Golden, Colorado, 80401

<sup>e</sup> National Institute of Standards and Technology, Material Measurement Laboratory, Division 642, 100 Bureau Drive, Gaithersburg, MD 20899

### ABSTRACT

Laser-assisted atom probe tomography (L-APT) was used to examine superconducting TiN/Ti/TiN trilayer films with nominal respective thicknesses of 5/5/5 (nm). Such materials are of interest for applications that require large arrays of microwave kinetic inductance detectors. The trilayers were deposited on Si substrates by reactive sputtering. Electron energy loss microscopy performed in a scanning transmission electron microscope (STEM/EELS) was used to corroborate the L-APT results and establish the overall thicknesses of the trilayers. Three separate batches were studied where the first (bottom) TiN layer was deposited at 500 °C (for all batches) and the subsequent TiN/Ti bilayer was deposited at ambient temperature, 250 °C, and 500 °C, respectively. L-APT rendered an approximately planar TiN/Si interface by making use of plausible mass-spectral assignments to N<sub>3</sub><sup>1+</sup>, SiN<sup>1+</sup>, and SiO<sup>1+</sup>. This was necessary since ambiguities associated with the likely simultaneous occurrence of Si<sup>1+</sup> and N<sub>2</sub><sup>1+</sup>

<sup>‡</sup> Contribution of NIST, an agency of the U.S. government; not subject to copyright in the United States.  
\* Corresponding author.  
*E-mail address:* sanford@boulder.nist.gov (N. A. Sanford)

prevented their use in rendering the TiN/Si interface upon reconstruction. The non-superconducting Ti<sub>2</sub>N phase was also revealed by L-APT and it was most prominent near the bottom Ti/TiN interface. Neither L-APT nor STEM/EELS rendered sharp Ti/TiN interfaces and the contrast between these layers diminished with increased film deposition temperature. L-APT also revealed that hydrogen was present in varying degrees in all samples including control samples that were composed of single layers of Ti or TiN.

## I. INTRODUCTION

Laser-assisted atom probe tomography (L-APT) is a relatively new metrology method that, *in principle*, will permit 3D chemical analysis of solid specimens and yield sub-nm spatial resolution with near-ppm sensitivity (Gault, et al., 2012; Larson, et al., 2013). L-APT studies of the superconducting TiN/Ti/TiN multilayer system are of interest in supporting development of microwave kinetic inductance detectors (MKIDs). Detectors fabricated from single-layer TiN films have been used in the past, however, TiN/Ti/TiN multilayers are a superior alternative (Vissers, et al., 2013a). Arrays of such multilayer detectors fabricated in our laboratory were used in the Balloon-borne Large Aperture Submillimeter Telescope (Galitzki, et al., 2014). Furthermore, L-APT can provide information on the distribution and concentration of the non-superconducting Ti<sub>2</sub>N phase, which is known to be problematic in these films (Vissers, et al., 2013b), and reveal suspected intermixing between Ti and TiN layers. Moreover, L-APT can also provide insight into H and O contamination in these structures. Interestingly, H and O have reportedly been found by L-APT analysis of Nb and these contaminants are

believed to degrade the performance of radio-frequency cavities fabricated from Nb and used in linear accelerators (Kim, et al., 2013; Kim, et al., 2015).

In practical L-APT analysis, errors and ambiguities arise in many instances and such issues may be functions of the structure and composition of the specimen at hand. For example, different laser-assisted ionic field-evaporation efficiencies between precipitates and the surrounding matrix were observed for certain high-strength steel alloys resulting in apparent increases in interfacial widths and changes in local densities (Mulholland and Seidman, 2011). In a completely different material system, L-APT of single-crystal GaN nanowires yielded non-physical Ga-rich or N-rich values for composition depending upon analysis conditions (Agrawal, et al., 2011; Diercks, et al., 2013; Sanford, et al., 2014). This latter example is of concern since, generally speaking, GaN only exists as a line compound and will decompose under slight deviations from perfect stoichiometry, i.e., 50 at.% Ga and 50 at.% (Okamoto, 2006). Given such caveats, L-APT studies should often be augmented with independent analyses in order to attach greater confidence to the results.

Composition rendering by L-APT is of particular concern for TiN since, in contrast to the GaN example described above, bulk TiN is known to be stable over a N composition fraction spanning roughly 30—50 at.% and can coexist with a Ti<sub>2</sub>N phase (Baker, 1992). Furthermore, we typically found that field evaporation from the TiN layers yielded TiN, Ti ions, and various other complexes. Consequently, use of L-APT in determining if the Ti/TiN interfaces are compositionally sharp, or graded, is problematic without separate measurements. Additionally, our L-APT instrument (flight length 90 mm) does not have the resolution to distinguish between N<sub>2</sub><sup>1+</sup> and Si<sup>1+</sup> since

both have a (dimensionless) mass-to-charge-state ratio at  $\approx 28$  Da.  $N^{1+}$ ,  $N_2^{2+}$  and  $Si^{2+}$  are similarly indistinguishable at 14 Da. Therefore, the ability of L-APT alone to correctly locate the TiN/Si interface, and thus measure the overall TiN/Ti/TiN trilayer thickness, is also problematic. As will be discussed at length in Section IV, ambiguities associated with locating the TiN/Si interface can be substantially mitigated by separately measuring the trilayer specimen thickness using scanning transmission electron microscopy (STEM). The overall aim of this paper is to illustrate details and methods associated with L-APT analysis of TiN/Ti/TiN multilayers and to serve as the starting point for the longer-term goal of optimizing such structures for MKID applications.

Following this introductory section, the paper is organized as follows: Section II describes deposition of TiN/Ti/TiN trilayer films and specimen preparation for analysis by L-APT, STEM, and STEM combined with electron energy loss microscopy (STEM/EELS). Fabrication and preparation of control specimens composed of single layers of TiN and Ti are also described. Section III discusses STEM/EELS procedures. Section IV presents L-APT experimental methodology, data analysis, and corroborating STEM/EELS experiments. A summary discussion is presented in Section V and concluding remarks appear in Section VI.

## II. SAMPLE PREPARATION

### A. Film deposition

TiN/Ti/TiN trilayer films were sputter-deposited onto Si substrates as follows: The substrates were high resistivity ( $\rho > 20$  k $\Omega$ -cm) Si wafers that were first immersed in an HF bath to strip off any surface oxide. The resulting H-terminated Si surface was

expected to remain stable long enough for the few minutes necessary to transfer the substrate to the sputtering chamber and initiate pump-down. Next, the substrate was heated to 500 °C and bombarded by an Ar-N plasma to form a  $\approx$  2 nm thick heavily-nitrided layer. The first TiN film was then deposited at 500 °C via reactive sputtering of a Ti target in the Ar-N plasma. The target was then shuttered; N<sub>2</sub> was removed from the gas stream, and the substrate was allowed to stabilize to the temperature desired for the subsequent sputter deposition of the Ti layer, which was then performed in an Ar plasma. When the desired Ti thickness was attained, the target was again shuttered, the substrate temperature stabilized as desired, N<sub>2</sub> reintroduced to the gas stream, and the terminal TiN layer deposited.

Control specimens consisting of single layers of TiN and Ti were also prepared by sputter deposition onto Si substrates. Both types of control specimens were subdivided into batches deposited at room temperature (RT) and 500 °C. The Si substrates for these specimens were prepared using the HF bath as described above, but the process of nitriding the Si surface prior to sputter deposition was omitted. Table I enumerates the specimen types used in this study and classifies them in terms layer thickness and deposition temperature.

#### B. Preparation of L-APT and STEM/EELS specimens by focused ion beam milling (FIB)

A protective 100 nm-thick Ni capping layer was deposited on each sample by e-beam evaporation prior to FIB processing. Fabrication of specimen tips for L-APT was then carried out in a dual-beam SEM/FIB system. First, standard lift-out techniques were used to mount slices of a sample wedge onto commercially-available silicon microposts (Thompson, 2007). Annular milling was then carried out at a FIB

acceleration voltage of 30 kV to progressively sharpen each wedge slice into a cone-shaped tip. Once the tip apex diameter was reduced to about 100 nm, milling at 5 kV was then used to form the final specimen shape shown in Figure 1(a).

Preparation of cross-sectional lamellae for STEM/EELS was also accomplished by FIB lift-out methods (Giannuzzi and Stevie, 1999). After mounting to a Cu micropost, each sample was thinned at 30 kV FIB acceleration voltage to a thickness of  $\approx 100$  nm. Final FIB milling was carried out at 5 kV to remove surface damage and further reduce the sample thickness.

### III. CHARACTERIZATION OF TiN/Ti/TiN TRILAYERS AND TiN MONOLAYERS BY STEM/EELS

EELS spectra were collected using an electron beam energy of 200 keV, a convergence angle of 22.7 mrad, and a collection angle of 55.6 mrad. Plural scattering was deconvolved from the core loss spectra (355 eV – 560 eV, 0.1 eV dispersion) using the zero loss peak (-20 eV – 185 eV, 0.1 eV dispersion) collected from the same area immediately following the core loss. Note that the EELS spectra were only quantified with respect to Ti and N. Hence, the analysis was performed to determine the relative concentration of Ti and N without providing a full quantitative composition of the sample in question.

### IV. L-APT DATA ACQUISITION AND ANALYSIS

#### A. Overview

All L-APT data acquisition was performed with a “LEAP 4000X Si” instrument manufactured by CAMECA and all data analysis was performed using the “IVAS 3.6.8” software provided by the same vendor (however, note the Disclaimer appearing near the end of the paper). This software was used to calculate three-dimensional reconstructions that, ideally, can map the identities and positions of atomic species in a specimen. The L-APT tool utilizes a pulsed laser that operates at 355 nm. The focused laser spot diameter at the specimen tip and the pulse duration were roughly 2  $\mu\text{m}$  and 8 ps, respectively.

Operational conditions of the L-APT tool were selected as a compromise to promote specimen longevity so that the data could be collected in a continuous fashion through the TiN/Ti/TiN trilayer film and into the Si substrate—without fracturing the specimen. Samples were generally run with the laser pulse energy (PE), pulse repetition rate, and detection rate (DR) in the respective ranges of 5—60 pJ, 250—500 kHz, and 0.2—0.5%. For all data acquisition cases considered, the pressure in the analysis chamber was within the range of 4—8 E-11 Torr and the specimen temperature was  $\approx 54$  K. Lower PE, specimen temperature, and increased DR would necessarily result in higher voltage applied to the specimen leading to an increased probability of fracture. PE settings in excess of 60 pJ were typically avoided since they were often associated with the onset of apparent “thermal tails” appearing in the mass-spectral peaks (Gault, et al., 2012; Larson, et al., 2013). For all reconstruction cases presented in this paper, an FESEM image of the specimen tip (acquired prior to L-APT data acquisition) was imported into the IVAS software to provide a direct measure of the specimen taper. Also, an FESEM image recorded after data acquisition was used to

estimate the IVAS “Sphere-Cone Radius Ratio” (S/C) reconstruction parameter for the same specimen. Note: in no case did we use the IVAS software option that computes the evolution of the tip radius based solely on the variation in the voltage applied to the specimen.

The reconstruction analysis requires assignment of the volumes occupied in the specimen by elemental constituents comprising the ionic species identified in the mass spectra. Table II lists assignments of ion types, corresponding volumes, and commentary on how these volumes were determined. Table III provides a summary listing of enumerated reconstructions accompanied by their respective data acquisition and analysis parameters. We remark that the reconstruction analysis parameters used in this paper do not necessarily represent a unique set per specimen examined. A discussion of the estimated uncertainties in the analysis procedure is presented in Section V. Further details pertinent to analysis of the different specimen types are presented next.

## B. Analysis of specimen type 1(a)

### (i) Specimen shape evolution during accumulation of mass-spectral data

For specimens of this type, the first TiN layer was deposited at 500 °C and the subsequent Ti and TiN layers were both deposited at ambient temperature. Results from IVAS analysis of this specimen type are well represented by reconstruction 2. Figures 1 (a, b) show the FESEM images of the specimen before and after L-APT data acquisition, respectively. Figure 2 shows how the voltage applied to the specimen can vary throughout the run in order to maintain a preset detection rate as ions are

progressively field-emitted away. Figure 3 (a) illustrates the accumulated mass spectrum that has been parsed to include a portion of the Ni cap layer, the entire TiN/Ti/TiN trilayer, and a portion of the Si substrate. Again, we adopt the convention where “Da” is defined as the normalized and dimensionless ratio of mass to charge. For example, the peak corresponding to the dominant isotope of  $\text{Ti}^{2+}$  appearing in Fig. 3 (a) should be centered (to the indicated precision) at 23.97 Da (Gault, 2012). For comparative purposes, Figs. 3 (b, c) illustrate mass spectra for the control samples consisting of TiN specimen type 2 (a) and Ti specimen type 3 (a), respectively. Evidence of Ga contamination from the FIB mounting process is typically found in all mass spectra and is associated with peaks near 69 Da and 71 Da. Peaks near 72 Da and 74 Da are assigned to  $\text{GaH}_3$ . Additional details are now clarified before presenting the composition analysis derived from reconstruction 2.

(ii) Thickness of the TiN/Ti/TiN trilayer

FIB was used to cut STEM/EELS lamella from regions of the host films that were roughly 3 mm from where the L-APT specimen tips were taken. This was a conservative precautionary measure to avoid material that may have been damaged by the prior FIB work that extracted the specimen tips. As noted in Table I, the full trilayer thicknesses of type 1 (a–c) specimens were measured by STEM and yielded 14 nm, 14 nm and 17 nm, respectively with an estimated uncertainty of  $\pm 0.2$  nm in each case. These overall trilayer thickness values were roughly 5 nm less than the associated values estimated from the assumed deposition rate of the sputtering tool.

(iii) Subtleties with volume assignments for Ti, N, and Si when calculating reconstructions

Knowledge of the volumes within a specimen that are occupied by elemental ions is required as input for the reconstruction analysis. However, there are ambiguities and uncertainties to contend with. For example, Ti ions appear in the mass spectra but we don't know what fraction of them originated from the separate Ti and TiN layers, or to what extent these layers may be intermixed. Consequently, volumetric uncertainties exist since it is unknown if the volume assignment per Ti ion detected should consider the density of Ti or TiN. Similar issues arise, but to a lesser extent, for other Ti-containing species, e.g., TiO, TiO<sub>2</sub>, and Ti<sub>2</sub>N, all of which were generally detected at concentrations much lower than Ti or TiN. Significantly, an incorrect choice of the volume contribution per Ti ion can force one to choose a non-physically large value of the IVAS "detector efficiency" (DE) fitting parameter when computing a reconstruction that returns a layer thickness in agreement with STEM/EELS measurements. As noted in Table II, the volume contributed to a reconstruction by a Ti ion originating from a Ti layer is 0.0177 nm<sup>3</sup> whereas a Ti ion (or a N ion) originating from a TiN layer contributes 0.00951 nm<sup>3</sup>. With the foregoing caveats in mind, we found that reconstructions of type 1(a) specimens were better represented by assigning 0.0177 nm<sup>3</sup> as the volume contribution per Ti ion. Reconstructions of all other TiN/Ti/TiN (which were deposited at elevated temperatures), and TiN specimens, were better represented by assigning a volume of 0.00951 nm<sup>3</sup> per Ti ion. More discussion of these points is presented in Section V.

Further ambiguities due to  $N^{1+}$ ,  $N_2^{1+}$ ,  $N_2^{2+}$ ,  $Si^{1+}$ , and  $Si^{2+}$  arise in assignments of peaks near 14 Da and 28 Da if one desires to carry the reconstruction analysis through the TiN/Si interface in one step. We point out that volumetric issues in these reconstructions can be substantially reduced if all such peaks are correspondingly assigned to  $N_2^{1+}$  and  $N_2^{2+}$ , and one exploits the fortuitous coincidence that the volume contributed by two N atoms originating from the TiN layer is  $0.0190 \text{ nm}^3$  and the volume contributed by a single Si atom originating from the Si substrate is  $0.0200 \text{ nm}^3$ . The  $N_2^{2+}$  assignment within the TiN/Ti/TiN trilayer is justified since, in spatially parsing the mass-spectral data to exclude the Si substrate (as guided by the trend in specimen voltage), we find that the observed isotopic ratios favor the  $N_2^{2+}$  assignments over  $N^{1+}$ .

Additionally, below the first TiN layer and into the Si substrate, the peak near 15 Da is given the fictitious assignment of  $N_2H_2^{2+}$  (diazene ion) however, its *actual* origin is interpreted to arise from  $SiH_2^{2+}$  (silylene ion). These ionic assignments and associated volumetric contributions are adopted purely for geometric scaling purposes and to permit generating reconstructions in one step without the need to parse the data into separate trilayer and substrate regions. However, while this scheme will maintain an approximately correct volume for the reconstruction across the TiN/Si interface, and is therefore useful in recovering the trilayer thickness, it will not, of course, eliminate compositional ambiguities between Si and N in this localized region.

(iv) Ionic species used to identify and render the TiN/Si interface

Mass-spectral assignments that could be ambiguously identified with either Si or  $N_2$  ions were not useful for identifying the TiN/Si interface. Therefore, signatures arising

from likely species that should be specific to the film/substrate interface were used to select the reconstruction analysis parameters instead. Given the unavoidable exposure of the Si substrates to ambient air prior film deposition, the  $\text{SiO}^{1+}$  assignment near 44 Da, which is apparently associated with the TiN/Si interface, is not unreasonable – even if the substrate had been transferred from the HF bath to the sputtering chamber in a time believed too short for oxidation of the Si surface to occur. If  $\text{SiO}_2$  was also present in the mass spectral data, it could not be distinguished from TiN. Additionally, prior to film deposition in the sputtering tool, the substrates were bombarded by a mixed N–Ar plasma that was intended to produce a N-rich Si surface and promote the subsequent growth of the first TiN layer. Therefore, it is also reasonable to assign peaks near 42 Da to either  $\text{SiN}^{1+}$  or  $\text{N}_3^{1+}$  (azide ion). We note that both of these have been spectroscopically studied in the gas phase species (Ojaha and Gopal, 2013; Hiraoka and Yamabe, 1989) and could form as gaseous species in the vicinity of the specimen tip during the process of ionic field emission. A minor peak at 70 Da offers ambiguous assignment to either  $\text{Si}_3\text{N}_4$  or GaH, but there are too few counts to convincingly place it at the TiN/Si interface and associate it with a nitrated Si surface.  $\text{SiH}_2$  ions (given the fictitious assignment of  $\text{N}_2\text{H}_2$  as described earlier) yield significant counts only in the substrate region and they diminish sharply as the interface is approached. Thus, the  $\text{SiH}_2$  ( $\text{N}_2\text{H}_2$ ) assignment provides an additional signature of the interface. Other ambiguous assignments involving likely species that appear localized near the TiN/Si interface could include  $\text{N}_2\text{O}$  (nitrous oxide) instead of SiO. As described next, we use such ionic species as markers to set up IVAS fitting parameters in order to yield reasonably planar TiN/Si interfaces. We again emphasize that such schemes are used

only to set up geometric reconstruction parameters and are not claimed to yield quantitative chemical information on the film/Si interface.

(v) 3D reconstructions and axial composition profiles

The primary constraints in selecting the reconstruction analysis parameters were that the IVAS software returns both the STEM determined thickness of the TiN/Ti/TiN trilayer and a reasonably planar TiN/Si interface. FESEM was used to measure the specimen tip shape before and after L-APT data acquisition thus providing estimates for the tip taper, the total length of material removed, and the S/C ratio—all of which were used as input to compute a reconstruction. The DE and image compression factor (ICF) were then varied to force the IVAS-rendered TiN/Si interface to be approximately planar and the thickness of the TiN/Ti/TiN trilayer to agree with the STEM estimate.

With items (i—iv) in mind, additional results for reconstruction 2 are now given. Figure 4 shows a 3D reconstruction that illustrates a portion of the Ni cap, the TiN/Ti/TiN trilayer, and the section of the Si substrate – all of which are encompassed within the voltage history described in Fig. 2. Figures 5 (a–c) show respective 2D views of isoconcentration (henceforth abbreviated as, “iso”) surfaces for SiO, SiN, and SiH<sub>2</sub>. These iso surfaces illustrate that the TiN/Si interface can be rendered approximately planar (for all three species) using the particular choice of analysis parameters used for reconstruction 2. Figure 6 (a) shows an axial concentration profile (in ionic %) for TiN, Ti, and H. We note the high concentration of H associated with the Ti layer. Figure 6 (b) shows an axial concentration profile (in atomic %) for Ti, N, H, Ni, and O where these species are counted as occurring both as elemental ions and as constituents

decomposed from molecular ions. Figure 6 (b) also indicates the spatial ambiguity in composition between Si and N near the TiN/Si interface. Figure 6 (c) shows the axial concentration profile (in ionic %) for  $Ti_2N$ , TiH, SiN, and  $SiH_2$ , where, as discussed earlier,  $SiH_2$  shares an ambiguous assignment with  $N_2H_2$ , and SiN shares an ambiguous assignment with  $N_3$ . The appearance of TiH in the Ti layer correlates with the high concentration of H species noted in the prior figures. Additionally, Fig. 6 (c) also indicates that the non-superconducting  $Ti_2N$  phase occurs at both TiN/Ti interfaces and that TiH is primarily concentrated in the Ti layer.

In many cases, the axis of the specimen tip is not precisely perpendicular with the film/Si interface nor is the reconstruction of the interface precisely planar. Therefore, as in Fig. 6 (a) and other similar figures, the axial Ti concentration profile does not drop immediately to zero as the interface is approached from the film side but may appear to require 1—2 nm to fall from its maximum to the noise level.

#### (vi) Comparison of L-APT with EELS

Using the representative case of reconstruction 2, a comparison of the axial concentration profiles of Ti and N measured by L-APT and EELS is given in Fig. 7 (a). Since EELS only recorded N and Ti, in order for the comparison with L-APT to be meaningful, H species, and the various other species occurring at relatively low levels, were excluded from the data in reconstruction 2 appearing in Fig 7 (a). The L-APT axial concentration profiles of Ti and N included contributions occurring both as elemental ions and as constituents decomposed from molecular ions. Figure 7 (a) illustrates that neither L-APT nor EELS rendered sharp Ti/TiN interfaces. Additionally, L-APT indicates

that Ti and N are present in roughly equal amounts in the TiN layers whereas EELS indicates the TiN layers are primarily Ti-rich except near the film surface and the substrate interface. Figure 7 (b) shows a representative cross-sectional STEM image of a type 1(a) specimen. The image encompasses a portion of the Ni cap, the full TiN/Ti/Ti trilayer, and a portion of the Si Substrate. The image does not resolve interfaces within the trilayer. Figure 7 (c) is a higher magnification of Fig. 7 (b) and illustrates that a lattice image of the Si substrate is evident but distinct interfaces between the Ti and TiN layers are not discernable. Hence, neither L-APT, STEM/EELS, nor cross-sectional STEM imaging resolved sharp interfaces between the TiN/Ti/TiN trilayer constituents. Trends in TiN/Ti interface resolution and layer composition exhibited by films deposited at elevated temperatures are described next.

### C. Analysis of specimen type 1(b)

We first present representative L-APT for this specimen type as derived from reconstruction 7 and then compare the results with EELS. It is unnecessary to repeat a detailed discussion similar to that given in B (i—iv), which described strategies used in setting up reconstructions for type 1(a) specimens. Similar considerations are implicit in all additional reconstruction analyses that follow.

Recall that for this specimen type the first TiN layer was deposited at 500 °C and the subsequent Ti and TiN layers were both deposited at 250 °C. Figure 8 (a) shows the variation in specimen voltage throughout the L-APT data acquisition process. Note, however, that the voltage does not display the sharp inflection associated with the first Ti/TiN interface that was seen in Fig. 2 for reconstruction 2 (for specimen type 1(a) ).

Figure 8 (b) illustrates the axial ionic concentration profile, but the appearance of a high concentration of H in the Ti layer is notably absent compared with Fig. 6 (a) for reconstruction 2. Figure 8 (c) shows the axial concentration profiles for the ambiguous respective pairs of molecular ionic species  $N_2H_2$ ,  $SiH_2$ ; and  $N_3$ ,  $SiN$ . As discussed earlier, all of these species may be plausibly associated with the TiN/Si interface. Additionally, it is reasonable to associate the  $N_3$  assignment with both the TiN top layer and the TiN/Si interface. Figure 8 (c) also shows how the non-superconducting  $Ti_2N$  phase is more widely distributed through both TiN layers rather than being localized to the TiN/Ti interfaces as was seen in Fig 6 (c) for reconstruction 2. Finally, the absence of significant H appearing in reconstruction 7 is consistent with a corresponding absence of TiH species in the mass spectrum—in contrast to what was observed for reconstruction 2.

The axial concentration profiles of N and Ti that were recorded by L-APT and EELS are compared in Fig. 9. The L-APT results originated from reconstruction 7 and are derived from both elemental species and decomposed from molecular ions. In this case, however, we retain the O and H species in displaying the L-APT data in order to illustrate that they occur at relatively low concentrations mostly near the surface of the specimen. Note that the EELS result in Fig. 9 again indicates Ti-rich character in the TiN regions, approximately equal Ti and N concentrations near the specimen surface, and also illustrates even less distinction between Ti and TiN layers than was seen in Fig. 7 for type 1 (a) specimens. Cross-sectional STEM fails to resolve interfaces between the layers deposited as TiN and Ti, but we omit these images for brevity. In the following section, we continue examining the comparative trends indicated by L-APT

and EELS for specimens of type 1(c) in which all films in the trilayer stack were deposited at 500 °C.

#### D. Analysis of specimen type 1(c)

Here again, we begin with a discussion of the L-APT analysis for this specimen type and then compare with EELS. Reconstruction 11 yielded representative results for this case. For brevity, we omit discussion of the ambiguous pairs of species SiN, N<sub>3</sub>; and N<sub>2</sub>H<sub>2</sub>, SiH<sub>2</sub> but mention that they were also used to set up the associated reconstruction parameters in a similar manner as described for the prior specimen types discussed. The variation in specimen voltage during data acquisition is shown in Fig. 10 (a). The voltage also lacks the sharp inflection associated with the first Ti/TiN interface discussed for reconstruction 2. Figure 10 (b) illustrates the axial concentration profile for ionic Ti and TiN. Note that in contrast to the preceding sample types, TiN is observed throughout the trilayer specimen, including the central layer that was deposited as Ti alone. Figure 10 (c) shows the ionic axial concentration profile of TiO<sub>2</sub>, H, and Ti<sub>2</sub>N. Compared to the prior specimen types, Ti<sub>2</sub>N occurs at a relatively higher concentration in the vicinity of the first TiN layer, H is concentrated in the top and bottom of the trilayer structure and a prominent concentration of TiO<sub>2</sub> is found near the specimen surface.

A comparison of the axial concentration profiles of N and Ti that were recorded by L-APT and EELS are shown in Fig. 11. Here, the L-APT result was derived from reconstruction 11 and the atomic concentrations included both elemental species and those decomposed from molecular ions. The results indicate that compared to

specimen types 1 (a, b), there is a reduced distinction between the three layers when all are deposited at 500 °C – indicating that chemical intermixing between the layers has occurred. Moreover, a comparison of the EELS results for the 3 types of trilayer samples generally yields an apparent Ti-rich composition except within a few nm of the surface. By contrast, L-APT indicates roughly equal Ti and N fractions in the regions deposited as TiN layers for specimen types 1 (a—c). These observations will be discussed at greater length in Section V.

#### E. Analysis of specimen type 2 (a)

Specimens of this type originated from a single TiN layer deposited to an intended thickness of 50 nm at room temperature. However, subsequent EELS analysis revealed the thickness to be 31 nm. As with the prior cases, the EELS specimen was cut from a region of the host film that was roughly 3 mm away from where the L-APT specimens originated. Representative L-APT results for this specimen type are given by reconstruction 13 and illustrated in Fig. 12 where axial concentration profiles of Ti, N, H, O, and Ni are illustrated. Here again, the atomic concentrations were derived from both elemental species and decomposed molecular ions. Both L-APT and STEM indicated that the Ti and N fractions are roughly equal throughout the film. H and O occur at a few atomic %, except near the Si interface and the top surface where they appear at roughly 5—7 at.%. The non-superconducting  $\text{Ti}_2\text{N}$  phase was present at  $\approx 0.5$  ionic % uniformly throughout the film but is omitted from the graph for brevity. EELS analysis for Ti and N is also superimposed on the L-APT results of Fig.

12. These results are now compared to a TiN control sample of similar thickness but deposited at 500 °C.

#### F. Analysis of specimen type 2 (b)

Specimens of this type originated from a single TiN layer deposited at 500 °C to a thickness of 40 nm as estimated by the sputtering system calibration. For this single case however, STEM/EELS returned the same thickness as the sputtering calibration. Reconstruction 17 yielded representative results which are shown as axial concentration profiles for Ti, N, H, O, and Ni as illustrated in Fig. 13. The indicated concentrations are derived from both elemental and decomposed molecular ions. Figure 13 shows both similarities and differences with the prior case given in Fig. 12. For example, both L-APT and EELS indicate that the Ti and N fractions are roughly equal throughout the bulk of the film. However, the L-APT results given in Fig. 13 show a greater concentration of both O and H in the vicinity of the film surface than was seen in Fig. 12. Additionally, the non-superconducting  $Ti_2N$  phase is distributed with the approximate respective ionic concentrations near the surface, in the bulk, and near the Si interface of 1%, 0.5%, and 0.7%. We next turn our attention to control samples composed of single Ti layers.

#### G. Analysis of specimen type 3 (a)

Specimens of this type originated from a single Ti layer deposited at room temperature to a thickness of 40 nm as estimated by the sputtering system calibration. Representative results are given by reconstruction 20. Figure 14 (a) gives a two

dimensional view of reconstruction 20. The coaxially placed cylinder is used to restrict a subset of the concentration analysis to the central portion of the reconstruction that is pertinent to Fig. 14 (c). Figure 14 (b) illustrates the axial concentration profiles for Ti, O, and H, as derived from elemental and molecular ions, for the entire reconstruction volume shown in Fig. 14 (a). Silicon is also detected at the periphery of the reconstruction (due to the curvature of the tip) and corresponds to the film/substrate interface. The results indicate significant O near the surface of the film that extends to a depth of roughly 10 nm. Additionally, H is present throughout the film and is most concentrated within a depth of 5—10 nm.

Figure 14 (c) shows axial atomic concentration profiles for Ti, O, and H that are restricted to the cylindrical volume shown in Fig. 14 (a). In this case the distribution of Ti, O, and H are quite similar to that shown in Fig. 14 (b), but the overall H concentration is reduced by roughly a factor of 2. Taken together, Figs. 14 (b, c) illustrate both an axial and radial dependence on the H distribution in the specimen. Our aim in examining these single-layer Ti films was to look for relative differences in H and O contamination between the RT and 500 °C deposition cases and not corroborate layer thickness with high precision. Therefore, neither specimen type 3 (a) nor type 3 (b), which is discussed next, were examined by STEM.

#### H. Analysis of specimen type 3 (b)

Specimens of this type originated from a single Ti layer deposited at 500 °C to a thickness of 50 nm as estimated by the sputtering system calibration. Representative results are given by reconstruction 22 and displayed as axial concentration profiles of

elemental and decomposed molecular ionic species illustrated in Figs. 15 (a, b). The results are quite similar to the prior cases shown in Figs. 14 (b, c) but there are some notable distinctions. For example, Fig. 15 (a) shows that H is more concentrated within a depth of 10-15 nm, and less distributed through the bulk of the film, compared to the counterpart case illustrated in Fig. 14 (b). Additionally, Fig. 15 (a) shows that the O-rich layer extends roughly 15 nm into the depth—which is roughly twice the depth that significant O was observed in the Ti film deposited at room temperature.

In Fig. 15 (b) the axial concentration analysis is confined to a cylinder 12.5 nm in diameter that is concentric with the full reconstruction. The trends for O and H are quite similar to those shown Fig. 15 (a), but Fig. 15 (b) indicates a comparatively reduced overall H concentration. Taken together, these observations again illustrate both axial and radial variations in H concentration similar to those observed for Ti films deposited at room temperature. A comparative discussion of the distribution of H revealed by L-APT in the various specimens examined will be taken up in section V that follows.

## V. DISCUSSION

### A. Issues associated with uncertainties in the IVAS reconstruction analysis

There are a number of factors that contribute to the uncertainties in the reconstruction analyses. For instance, FESEM imaging of the specimen obtained prior to L-APT was imported into the IVAS software since instrumental constraints prevented the use of TEM imaging to more precisely measure the specimen shape and residual thickness of the Ni cap. We estimate that the FESEM image contrast between the Ni

cap and the TiN top layer introduces an uncertainty of  $\pm 5$  nm in locating the Ni/TiN interface, and roughly the same uncertainty in diametric measurements used to measure the specimen taper. The S/C parameter was only available for evaluation (on intact specimens) after L-APT progressed into the Si substrate, and given the variation in specimen voltage and the conical shape, there is no *a priori* reason to assume that the S/C parameter should be the same in both the film and substrate regions. Consequently, S/C is better regarded as an adjustable parameter with its initial estimate measured by FESEM. With these caveats in mind, our estimated measurement uncertainty in S/C is typically  $\pm 5$  %.

This collection of uncertainties propagated into the reconstruction analysis as follows: With initial values of the Ni/film interface position and S/C assumed correct, the ICF and DE were varied until IVAS returned the separately-measured film thickness and rendered an approximately planar film/Si interface. If these constraints were not met, the process was iterated (by varying ICF, DE, S/C, and Ni/film interface position) until they were.

The issue of setting the DE parameter deserves more attention as far as consequences on reconstruction uncertainties are concerned. In particular, the fractional active area available on the installed detector is  $\approx 0.6$  and the actual detector efficiency cannot exceed this value even in the most optimal conditions. Therefore, a reconstruction analysis that returns the expected thickness and planar interfaces, but requires a value of  $DE > 0.6$ , may indicate that an incorrect choice of volume per elemental species was assumed. Such considerations were discussed in section IV [B

(iii) ] and helped guide our assignment of the volume contributed per Ti atom for specimen type 1 (a—c).

Finally, we note that the reconstructions per specimen type as summarized in Table III are remarkably similar regardless of laser PE used. Thus, the spans of DE, ICF, and S/C may be regarded as approximate resulting uncertainties in these fitted quantities for a particular specimen type under consideration. However, given the multivariate nature of the reconstruction fitting process, we emphasize that the fitted parameters given in Table III by no mean necessarily represent unique solutions for their respective cases.

#### B. The presence of hydrogen in the specimen films

Recent L-APT studies of Nb that used a tool, and operational conditions, very similar to ours have shown H concentrations in the range of  $\approx 20$ —50 at.% (Kim, et al., 2013; Kim, et al., 2015). Notably, however, Kim et al. (2013, 2015) also equipped their tool with a residual gas analyzer (RGA) to separately measure the H species in their chamber. This added RGA functionality enabled them to conclude that the detected H originated from the specimen and not chamber background. By extension, it is therefore reasonable to expect that the H concentrations in the Ti layers for type 1(a) specimens, as illustrated in Figs. 6(a, b), are primarily from the specimen and not chamber background. Moreover, the binary phase diagram for the bulk Ti-H system indicates that a H concentration of roughly 60 at.% at RT is not unexpected (Baker, 1992). Uptake of H by the Ti layers could take place via multiple pathways, e.g. during

film deposition, after deposition and exposure to ambient air, as a consequence of FIB processing, or some combination of such factors.

A comparison of the H concentrations observed in the various specimen types reveals both distinctions and similarities between cases where the Ti layers were deposited at RT, or deposited at elevated temperatures. Considering RT examples first: Reconstructions of the Ti layers in type 1 (a) specimens display the highest apparent concentrations of H ( $\approx 45\text{--}65$  at. %) which are roughly 2—3 times greater than those measured in the type 3 (a) Ti (control) specimens. Additionally, reconstructions of both specimen types show axial concentrations of H that peak toward the film surface. For the type 1 (a) specimens, the maximum H concentration occurs near the upper TiN/Ti interface. For reconstructions of the type 3 (a) specimens, the maximum H concentration occurs near the interface region between the oxidized surface layer and the bulk Ti film. Such an axially asymmetric concentration profile may arise via H ion migration under the combined effects of laser heating and the strong electric field present during L-APT.

A radial variation in H concentration in the reconstructions of type 3 (a) specimens is also seen in comparing Figs. 14 (b, c). These figures illustrate that the axial H concentration confined to the coaxial cylinder illustrated in Fig. 14 (a) is roughly a factor of 2 less than the axial concentration along the full diameter of the reconstruction. Such a radial gradient H concentration may exist as a H diffusion artifact prior to L-APT, arise from ion migration as described above, or result from some combination thereof. Similarly, the H concentrations in the Ti layers near the reconstruction centers of the type 1 (a) specimens are roughly a factor of 2 less than

near the reconstruction sidewalls. Finally, the radial variations in H distributions were seldom azimuthally uniform in any specimen examined, which may indicate that the unavoidable non-uniform laser heating over the specimen surface could also play a role.

Reconstructions of Ti layers deposited at elevated temperatures yielded greater H concentrations compared to Ti layers deposited at RT. For example, the H concentrations in the Ti-deposited regions of specimen types 1 (b) and (c) are only a few at. % compared to the  $\approx 45\text{--}65$  at.% H concentrations for type 1 (a). Similar trends, but of lower magnitude, are seen in comparing reconstructions of the Ti control samples. Specifically, the integrated H concentration for reconstruction 20 (Ti deposited at RT) is  $\approx 6.6$  at.% and the integrated H concentration for reconstruction 22 (Ti deposited at  $500\text{ }^\circ\text{C}$ ) is  $\approx 3.5$  at.%. In making these comparisons, the H counts include those derived from atomic species and those decomposed from molecular ions.

### C. Comparison of EELS and L-APT results

Neither EELS nor L-APT render sharp interfaces between Ti and TiN layers in any of the type 1 (a—c) trilayer specimens regardless of film deposition temperature. For specimen types 1 (a) and (b), EELS shows Ti-rich concentrations in regions deposited as TiN except in the vicinities of the Ni cap and Si substrate where EELS shows roughly equal Ti and N concentrations. These effects are illustrated in Figs. 7 (a) and 9, respectively. For the type 1 (c) specimen, EELS shows a Ti-rich concentration throughout the entire trilayer. By contrast, L-APT on types 1 (a—c) generally show Ti-rich concentrations only in the regions deposited as Ti. Additionally, as seen in Figs. 12 and 13, both EELS and L-APT give approximately equivalent Ti and N concentrations in

both TiN control specimen films that were deposited at RT and 500 °C, respectively. Consequently, it is not immediately clear if the EELS results that indicate a general tendency for Ti-rich concentrations in the TiN layers in all three of the type 1 specimens are physical properties of the films or measurement artifacts. Finally, we estimate that the uncertainty in registration of the EELS and L-APT axial concentration profiles is approximately  $\pm 2$  nm.

Even with lingering uncertainties regarding the absolute chemical compositions of the layers as revealed by L-APT and EELS, both methods show that the TiN/Ti/TiN interfaces are not abrupt for the film thickness ranges and processing temperatures we indicate. Moreover, as illustrated in Figs. 7 (b, c), cross sectional STEM resolves no interfaces for TiN/Ti layers deposited at RT. On the other hand, the phase diagram for bulk TiN suggests that such Ti/TiN layer intermixing should be negligible below  $\approx 500$  °C (Baker, 1992) and this is consistent with thermal stability studies of thicker (66 nm/76 nm/80 nm) TiN/Ti/TiN trilayer structures as discussed by Wang and Allen (1996).

The apparent intermixing of the TiN/Ti interfaces in our (thinner) trilayer samples imply possible mechanisms such as the existence of a metastable Ti-rich TiN phase, and that N is soluble interstitially in Ti even at RT. We note that RT diffusion of N into Ti has been discussed by other workers (Siew, et al., 2001; Dawson and Tzatzov, 1987). Our EELS and L-APT results both indicate that the layers become progressively less distinct in comparing the RT, 250 °C, and 500 °C film deposition temperatures. Taken together, these results suggest that with the Ti and TiN layer thicknesses under discussion, layer intermixing can occur at temperatures  $< 500$  °C.

## VI Conclusions

Laser-assisted atom probe tomography (L-APT) revealed that the interfaces between sputter-deposited Ti and TiN films in TiN/Ti/TiN trilayer superconducting films undergo nanoscale intermixing even if the films were deposited at room temperature. Progressively increased intermixing occurred in specimens prepared at the deposition temperatures of 250 °C and 500 °C. The apparent intermixing effects were corroborated by STEM/EELS. Additionally, L-APT showed a spatially-varying, concentration of H ( $\approx$  20—50 at.%) in the RT-deposited Ti layers of the trilayer specimens. However, L-APT found that H was comparatively absent in the Ti layers of trilayer samples deposited at the higher temperatures. Additionally, L-APT showed that the non-superconducting  $\text{Ti}_2\text{N}$  phase was present in all trilayer specimens examined. Film deposition on Si substrates introduced ambiguities in the mass spectral assignments, and complications in the L-APT data reconstruction analysis, that could be mitigated by separate STEM/EELS measurement of film thickness, and mass spectral assignments of species plausibly localized to the trilayer/Si interfaces.

#### Disclaimer

Identification of certain vendors, products, software, or services does not constitute an endorsement by the National Institute of Standards and Technology. Alternatives supplied from other sources may prove to be similar or superior.

## Acknowledgements

We gratefully acknowledge useful discussions with Ann Chiaramonti Debay.  
This work received support from the National Institute of Standards and Technology.  
The contribution of D. R. Diercks was supported by the Colorado School of Mines.

## References

- Agrawal, R, Bernal, R.A., Isheim, D., Espinosa, H.D., 2011. Characterizing atomic composition and dopant distribution in wide band gap semiconductor nanowires using laser-assisted atom probe tomography. *J. Phys. Chem. C* 115, 17688—17694.
- American Elements, Silicon Monoxide Properties.  
<https://www.americanelements.com/silicon-monoxide-10097-28-6> (accessed 16.12.04)
- Baker, H., Editor, 1992. *ASM Handbook, Volume 3, Alloy Phase Diagrams*, ASM International, Materials Park, Ohio.
- Dawson, P.T., Tzatzov, K.K., 1987. Nitrogen sorption on titanium: Reconstruction of the subsurface composition profile using low- and high-energy Auger data. *J. Vac. Sci. Technol. A* 5(4), 1345—1351.
- Diercks, D.R., Gorman, B.P., Kirchhofer, R., Sanford, N. Bertness, K. Brubaker, M., 2013. Atom probe tomography evaporation behavior of C-axis GaN nanowires: Crystallographic, stoichiometric, and detection efficiency aspects. *J. Appl. Phys.* 114, 184903.
- Galitzki, N., Ade, P.A.R., Angil`e, F.E., Ashton, P., et al., 2014. The next generation BLAST experiment. *J. Astron. Instrum.* 3, 1440001.
- Gault, B., Moody, M.P., Cairney, J.M., Ringer, S.P., 2012. *Atom Probe Microscopy*, Springer, New York.
- Giannuzzi, L.A., Stevie, F.A., 1999. A review of focused ion beam milling techniques for TEM specimen preparation. *Micron* 30, 197—204.
- Hiraoka, K, Yamabe, S., 1989. Stabilities of the  $N_3^+(N_2)_n$  cluster ions with  $n = 1—11$ . *Chem. Phys. Lett.* 154(2), 139—142.
- International Centre for Diffraction Data, Powder Diffraction File™.  
<http://www.icdd.com/> (accessed 13.05.16)
- Kim, Y.-J., Seidman, D.N., 2015. Atom-probe tomographic analyses of hydrogen interstitial atoms in ultrahigh purity niobium. *Microsc. and Microanal.* 21, 535—543.
- Kim, Y.-J., Tao, R., Klie, R.F., Seidman, D.N., 2013. Direct atomic-scale imaging of hydrogen and oxygen interstitials in pure niobium using atom-probe tomography and aberration-corrected scanning transmission electron microscopy. *ACS Nano* 7, 732—739.
- Larson, D.J., Prosa, T.J., Ulfing, R.M., Geiser, B.P., Kelly, T.F., 2013. *Local Electrode Atom Probe Tomography*, Springer, New York.

Mulholland, M.D., Seidman, D.N., 2011. Voltage-pulsed and laser-pulsed atom probe tomography of a multiphase high-strength low-carbon steel. *Microsc. and Microanal.* 17, 950—962.

Ojha, K.S., Gopal, R., 2013. Laser Induced Spectra of SiN molecule in near IR region. *Int. J. Spectros.*, article ID 915365.

Okamoto, H., 2006. Ga-N (Gallium-Nitrogen). *Phase Equilib. Diffusion* 27(5), 545—546.

Sanford, N.A., Blanchard, P.T., Bertness, K.A., Roshko, A., Schlager, J.B., Kirchhofer, R., Diercks, D.R., Gorman, B., 2014. Laser-assisted atom probe tomography of MBE grown GaN nanowire heterostructures. *Phys. Status Solidi C* 11(3-4), 608—612.

Siew, H.L., Qiao, M.H., Chew, C.H., Mok, K.F., Chan, L., Xu, G.Q., 2001. Adsorption and reaction of NH<sub>3</sub> on Ti/Si(1 0 0). *Appl. Surf. Sci.* 173, 95—102.

Thompson, K., Lawrence, D., Larson, D.J., Olson, J.D., Kelly, T.F. Gorman, B., 2007. In situ site-specific specimen preparation for atom probe tomography. *Ultramicroscopy* 107, 131—139.

Vissers, M.R., Gao, J., Sandberg, M., Duff, S.M., Wisbey, D.S., Irwin, K.D., Pappas, D.P., 2013a. Proximity-coupled Ti/TiN multilayers for use in kinetic inductance detectors. *Appl. Phys. Lett.* 102, 232603.

Vissers, M.R., Gao, J., Kline, J.S., Sandberg, M., Weides, M.P., Wisbey, D.S., Pappas, D.P., 2013b. Characterization and in-situ monitoring of sub-stoichiometric adjustable superconducting critical temperature titanium nitride growth. *Thin Solid Films* 548, 485—488.

Wang, S.-Q., Allen, L.H., 1996. Thermal stability of  $\alpha$ -titanium in contact with titanium nitride. *J. Appl. Phys.* 79, 2446—2457.

film	specimen type	TiN		Ti		TiN		L <sub>s</sub>	
		L	T	L	T	L	T		
TiN/Ti/TiN trilayer	1	a	5	500	10	RT	5	RT	14
		b	5	500	10	250	5	250	14
		c	5	500	10	500	5	500	17
TiN monolayer	2	a	50	RT	-	-	-	-	31
		b	40	500	-	-	-	-	40
Ti monolayer	3	a	-	-	50	RT	-	-	-
		b	-	-	50	500	-	-	-

Table I. Specimen film deposition schedule. L is the intended layer thickness in nm based on the sputtering system calibration, T is the deposition temperature in °C, and RT indicates deposition at room temperature. The layer deposition sequence for specimens 1 (a–c) reads left-to-right. The full specimen thickness in nm as measured by STEM is indicated by L<sub>s</sub>. The uncertainty in L<sub>s</sub> was estimated to be ±0.2 nm in each case.

Block	origin of $v$	species	$v$ ( $\times 10^{-2} \text{ nm}^3$ )	notes
1	ICDD	Ti	1.77	used for specimen 1(a) reconstructions
		TiH	1.77	
		TiN	1.90	
		Ti <sub>2</sub> N	3.78	
		TiO	1.82	
		TiO <sub>2</sub>	3.10	
		Ti <sub>2</sub> O <sub>3</sub>	–	
2	TiN	Ti	0.951	used for specimen 1(b, c), 2(a, b) reconstructions
		N, NH <sub>3</sub>	0.951	ambiguity with Si <sup>2+</sup>
		N <sub>2</sub> , N <sub>2</sub> H <sub>2</sub>	1.90	ambiguity with Si, SiH <sub>2</sub>
3	AE	SiO	3.44	SiO density: 2.13 g/cm <sup>3</sup>
	TiN, TiO	N <sub>2</sub> O	2.81	Likely gaseous specie
4	IVAS	C	0.878	minor; origin unknown
		GaH <sub>3</sub> , GaH, Ga	1.96	Ga residue from FIB mostly isolated near specimen tip.
		H <sub>3</sub> , H <sub>2</sub> , H	0.00	H contributes no volume
		Si, SiH <sub>2</sub>	2.00	ambiguities with N <sub>2</sub> , N <sub>2</sub> H <sub>2</sub>
5	Si, TiN	SiN	2.95	assumed gaseous specie
	TiN	N <sub>3</sub>	2.85	assumed gaseous specie

Table II. Volumetric contribution  $v$  of ionic species with notes regarding ambiguous assignments and other clarifications. For brevity, the charge states are not labeled. In all cases it is assumed that H contributes no volume to a reconstruction. Block 1:  $v$  for Ti, and related Ti complexes were derived using the International Centre for Diffraction Data (ICDD), Powder Diffraction File™, (2013). If present, Ti<sub>2</sub>O<sub>3</sub> would contribute insignificant  $v$  but its possible appearance is ambiguous with a likely GaH<sub>3</sub> assignment. Block 2:  $v$  for TiN was used to calculate the corresponding volumetric contributions of Ti and N that originated from a TiN ion. The choice of  $v$  for Ti, as originating from the Ti layer or the TiN layer, is discussed in the text. Block 3:  $v$  corresponding to an SiO ion was calculated using data available from American Elements (AE), (2016). The value of  $v$  corresponding to an N<sub>2</sub>O ion was calculated using the volume contribution of O from TiO (Block 1) and the contribution of N from TiN (Block 2). Block 4: IVAS-default values of  $v$  for C, Ga, and Si. Since the volumetric contributions of Ga and C are negligible at the detected concentrations, there is no loss of generality using these default values. Block 5: The values of  $v$  for SiN and N<sub>3</sub> ions were computed by using the  $v$  contributions obtained for N and Si from Blocks 2 and 4, respectively. Note, however, that both SiN and N<sub>3</sub> are presumed to be gaseous species (Ojha and Gopal, 2013; Hiraoka and Yamabe, 1989) that have formed during field emission. Additionally, neither O<sup>1+</sup> nor O<sub>2</sub><sup>2+</sup> can be unambiguously distinguished from a Ti<sup>3+</sup> peak near 48 Da and that O<sub>2</sub><sup>1+</sup> near 32 Da is ambiguous with TiN<sup>2+</sup>.

specimen type	reconstruction	PE (pJ)	DR	DE	ICF	S/C	ID
1(a)	1	20	0.4	0.38	1.65	1.37	(1-6)00976v09
	2	25	0.4	0.41	1.72	1.35	(1-7)00977v10
	3	30	0.4	0.38	1.70	1.33	(1-9)00979v09
	4	30	0.2	0.37	1.65	1.33	(1-1)00971v04
1(b)	5	15	0.3	0.55	1.30	1.25	(1-6)01335v11
	6	20	0.3	0.58	1.40	1.24	(1-2)01331v06
	7	30	0.4	0.60	1.40	1.20	(1-1)01330v16
	8	50	0.3	0.60	1.30	1.15	(2-3)01338v07
1(c)	9	5	0.3	0.53	1.40	1.22	(1-6)01356v08
	10	20	0.3	0.48	1.35	1.39	(1-2)01352v06
	11	30	0.4	0.56	1.50	1.25	(1-1)01350v23
	12	50	0.3	0.60	1.40	1.15	(2-3)01359v03
2(a)	13	50	0.5	0.58	1.40	1.15	(6-1)01653v10
	14	55	0.5	0.57	1.40	1.06	(5-3)01655v05
	15	60	0.4	0.58	1.50	1.07	(6-2)01652v10
2(b)	16	20	0.3	0.41	1.85	1.08	(2-5)01690v02
	17	30	0.3	0.35	1.80	1.15	(2-3)01689v06
	18	55	0.3	0.55	1.20	1.15	(2-9)01692v05
	19	60	0.3	0.51	1.35	1.05	(2-1)01687v01
3(a)	20	30	0.3	0.49	1.60	1.10	(2-5)01848v07
	21	40	0.4	0.50	1.90	1.04	(2-4)01847v04
3(b)	22	30	0.3	0.50	2.0	1.28	(1-2)01876v01
	23	50	0.4	0.60	1.9	1.4	(2-2)01884v01

Table III. Instrumental and analysis parameters per reconstruction. The laser pulse energy and data detection rate are indicated by PE, and DR, respectively. All specimens were examined using a laser repetition rate of 250 kHz, except for reconstruction 4 which used 500 kHz. In all cases, the specimen-detector flight length and specimen temperature was 90 mm and 54 K, respectively. All reconstructions were computed using the “Tip Profile” option in the IVAS software. In Tip Profile, an FESEM image of the specimen recorded prior to L-APT was imported into the code, and an image recorded after L-APT was used to estimate the IVAS “Sphere-Cone Radius Ratio” parameter abbreviated as S/C. The associated parameters, “Detector Efficiency” and “Image Compression Factor,” are indicated by DC and ICF, respectively.

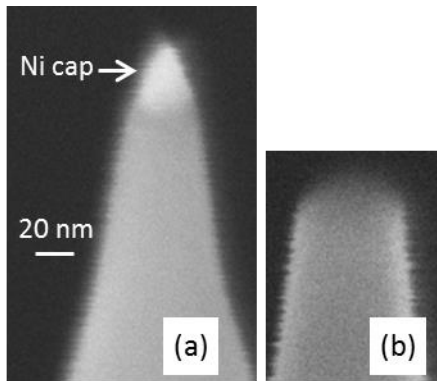


Fig. 1. FESEM images before and after L-APT of the specimen tip corresponding to reconstruction 2. (a) Tip before L-APT illustrating the protective Ni cap. The tip is tilted toward the observer with its long axis oriented at  $54^\circ$  from the horizontal. (b) Same tip after L-APT but viewed with zero tilt with its long axis oriented at  $90^\circ$  from the horizontal.

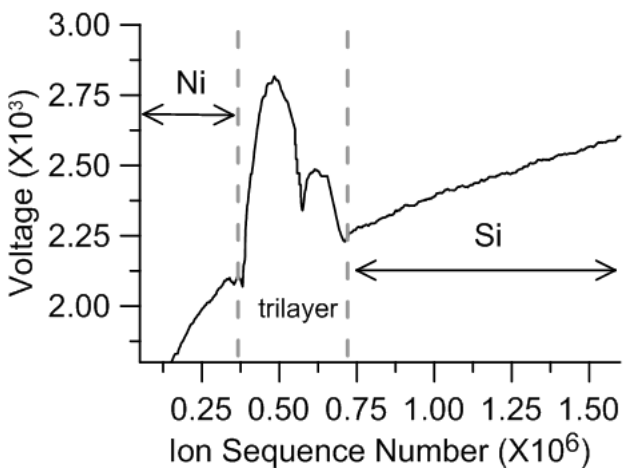


Fig. 2. Variation in specimen voltage for example of reconstruction 2. The voltage is seen to change abruptly as the field evaporation process proceeds through the Ni cap, trilayer, and into the Si substrate. Note the sharp voltage inflection near Ion Sequence Number  $\approx 0.6 \times 10^6$  which corresponds to the first Ti/TiN interface.

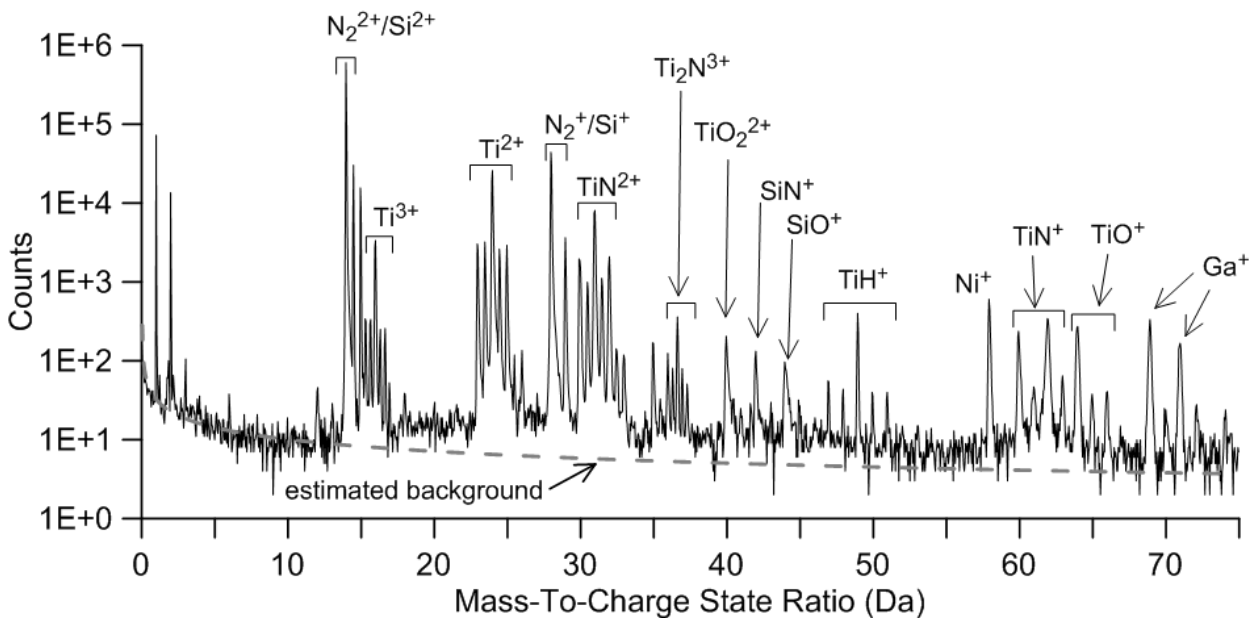


Fig. 3 (a). Elemental and molecular ionic species in the accumulated mass spectrum corresponding to TiN/Ti/TiN sample type 1 (a), reconstruction 2. For brevity, not all peak assignments and charge states are labeled. The data is parsed to omit most of the Ni cap layer but includes portion of the Si substrate. There are numerous ambiguous assignments including peaks near 14 Da and 28 Da which could be assigned to  $N_2$  or Si ions as indicated. Other plausible ambiguous assignments discussed in the text include  $N_2H_2$  with  $SiH_2$ , and  $N_3$  with  $SiN$ .

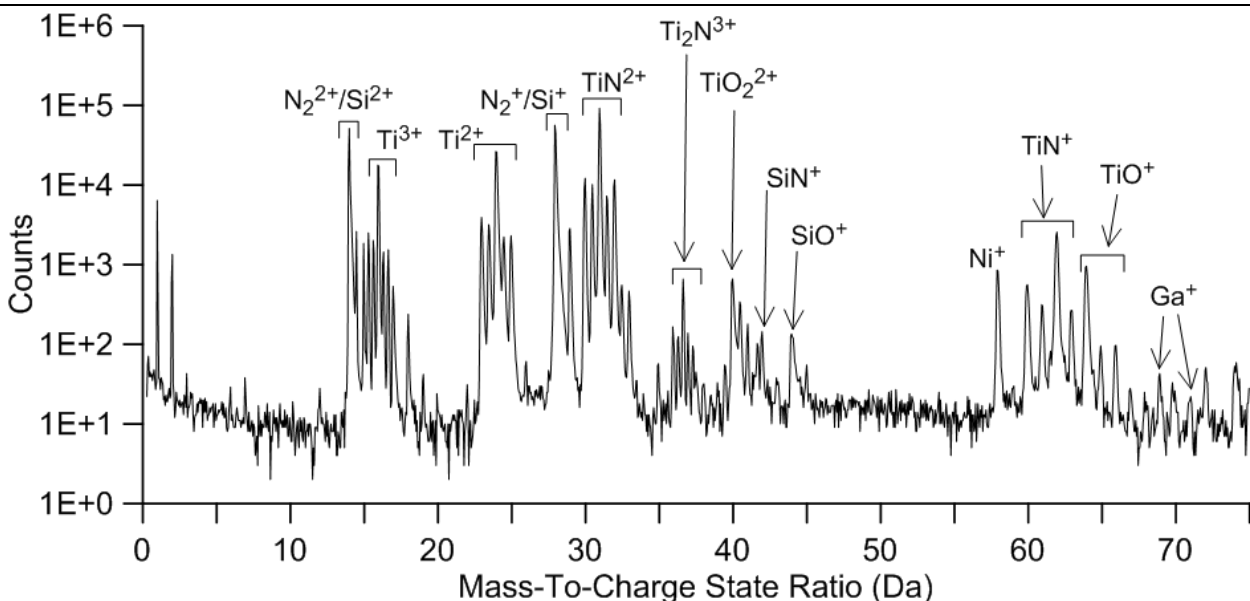


Fig. 3 (b). Elemental and molecular ionic species in the accumulated mass spectrum corresponding to TiN sample type 2 (a), reconstruction 13. The mass spectrum is quite similar to (a) with the notable exceptions that TiH assignments near 50 Da are absent and Ga contamination is far less prominent.

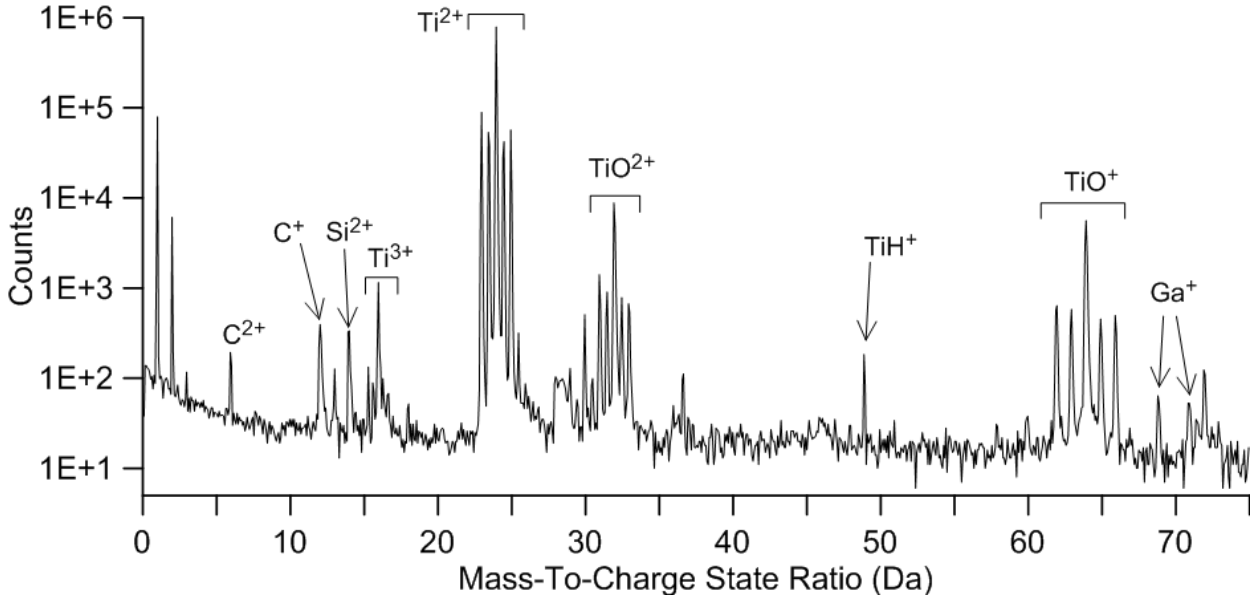


Fig. 3 (c). Elemental and molecular ionic species in the accumulated mass spectrum corresponding to Ti sample type 3 (a), reconstruction 20. The mass spectrum is dominated by Ti and TiO species. Peaks observed near 80 Da are assigned  $TiO_2$  but are omitted for brevity since they only occur concentrations comparable to the Ga contamination shown.

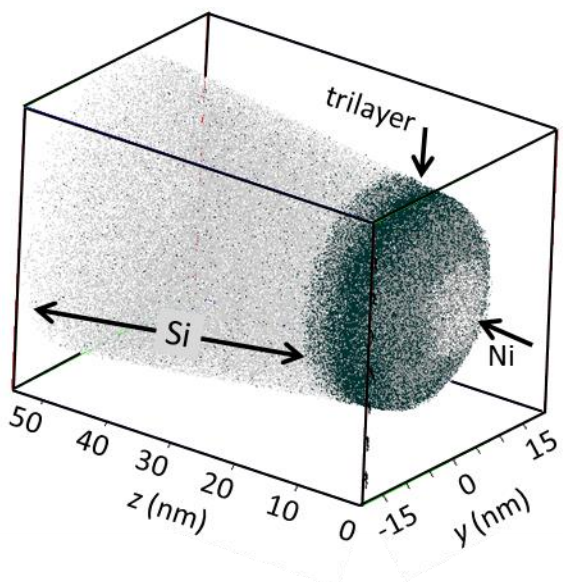


Fig. 4. 3D view of reconstruction 2. A remnant portion of the Ni cap, the TiN/Ti/TiN trilayer region, and the Si substrate are indicated.

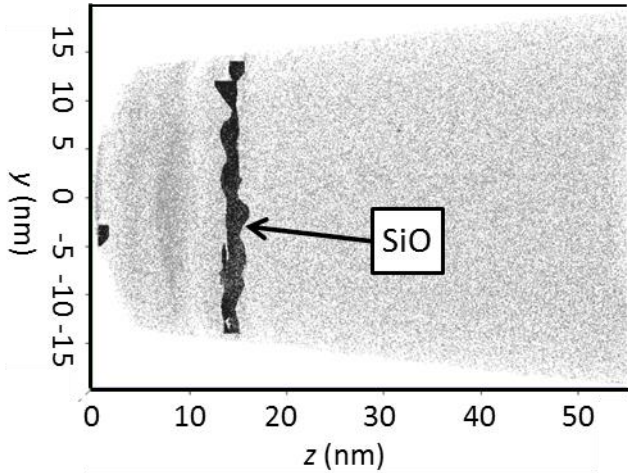


Fig. 5 (a). Isoconcentration surface of SiO computed for reconstruction 2. The concentration of SiO represented is 1.1 ionic % and is coincident with the TiN/Si interface. As described in the text, SiO is not a unique assignment but is ambiguous with the likely presence of N<sub>2</sub>O at this interface.

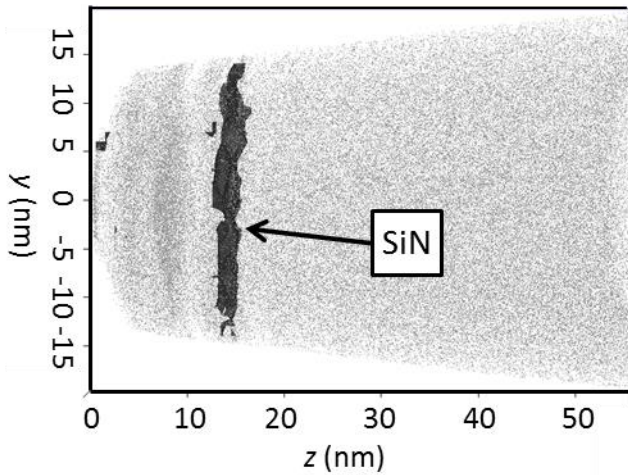


Fig. 5 (b). Isoconcentration surface of SiN computed for reconstruction 2. The concentration of SiN represented is 1.0 ionic % and is coincident with the TiN/Si interface. As described in the text, SiN is not a unique assignment but is ambiguous with the likely presence of N<sub>3</sub> at this interface.

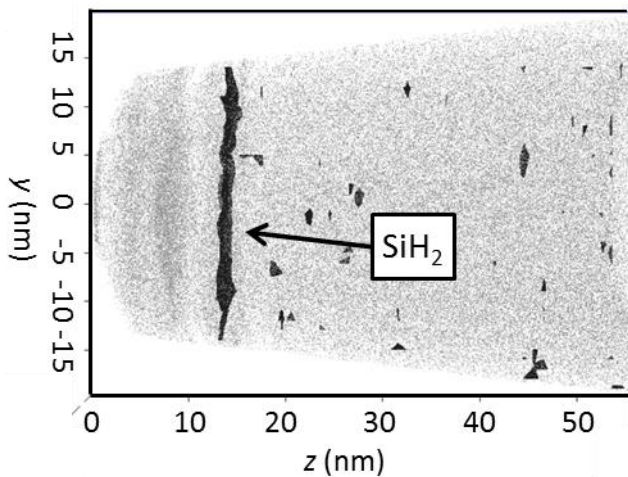


Fig. 5 (c). Isoconcentration surface of SiH<sub>2</sub>, as represented by the alias assignment to N<sub>2</sub>H<sub>2</sub>, computed for reconstruction 2. The concentration of N<sub>2</sub>H<sub>2</sub> represented is 1.24 ionic % and is coincident with the TiN/Si interface.

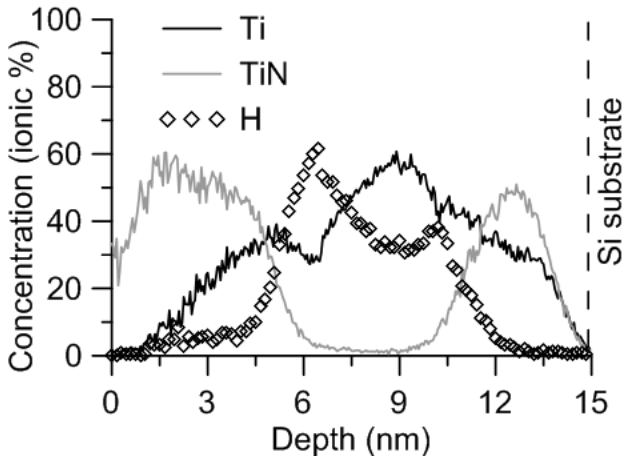


Fig. 6 (a). Axial concentration profile of Ti, TiN, and H ionic species for reconstruction 2. The result indicates significant H concentration associated with the Ti layer.

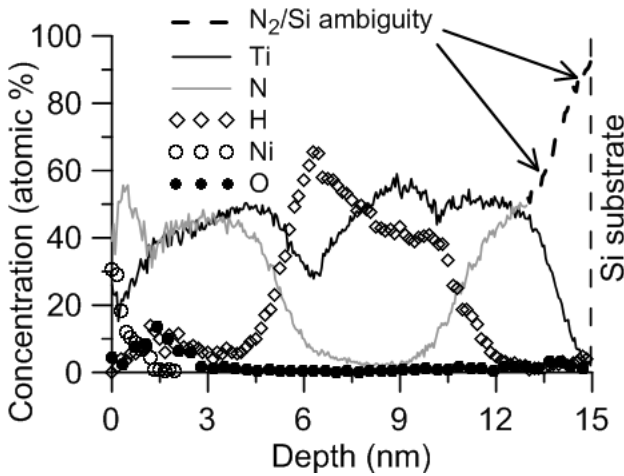


Fig. 6 (b). Axial concentration profile of Ti, N, H, Ni, and O atomic species, present both as elemental ions and decomposed from molecular ions, as derived from reconstruction 2. The results show the unavoidable ambiguity between assignments of N and Si species near the TiN/Si interface. The data has been parsed to include a remnant of the Ni cap.

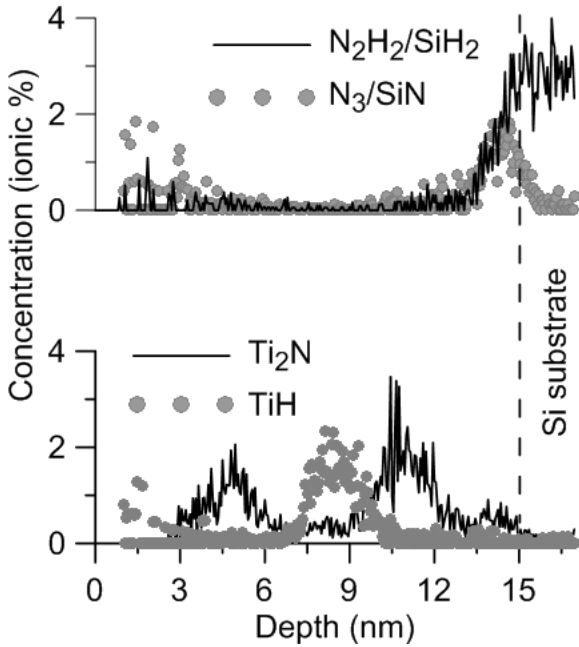


Fig. 6 (c). Results for both upper and lower portions of the graph are derived from reconstruction 2. Upper portion: Axial concentration profile for the ambiguous respective pairs of molecular ionic species  $N_2H_2$ ,  $SiH_2$ ; and  $N_3$ ,  $SiN$ . All may be plausibly associated with the TiN/Si interface as described in the text. Additionally,  $N_3$  may plausibly originate from the top TiN to a depth of roughly 3 nm. Lower portion: Axial concentration profile of  $Ti_2N$  and  $TiH$  molecular ionic species. The non-superconducting  $Ti_2N$  phase appears to be localized near both upper and lower TiN/Ti interfaces.  $TiH$  is primarily associated with the Ti layer

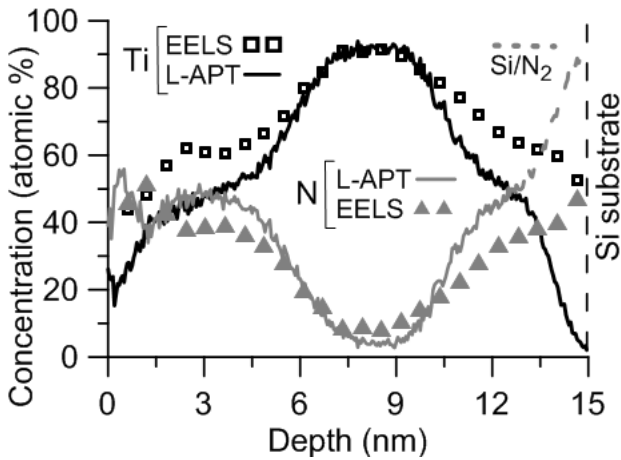


Fig. 7 (a). Comparative axial concentration profile of Ti and N atomic species as measured by L-APT and EELS. The L-APT result is derived from reconstruction 2 where the H counts have been excluded and Ti and N counts originate from both elemental and decomposed molecular ions. Neither L-APT nor STEM/EELS indicate sharp interfaces between Ti and TiN layers. The ambiguous L-APT assignment between Si and N species near the TiN/Si interface is indicated. Residual Ni and other species present near the specimen surface are omitted for clarity thus the Ti and N counts do not sum to 100%.

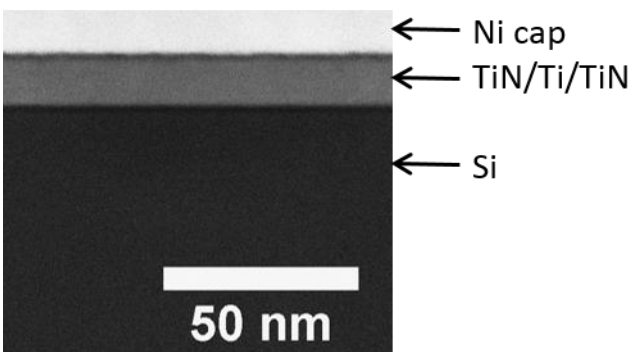


Fig. 7 (b). STEM cross sectional image of a lamella cut from specimen of type 1 (a). Contrast is evident between the Ni cap and the upper TiN layer, and between the Si substrate and the lower TiN layer. No image contrast can be resolved between the Ti and TiN layers. The image is cropped so the full thickness of the Ni cap is not shown.

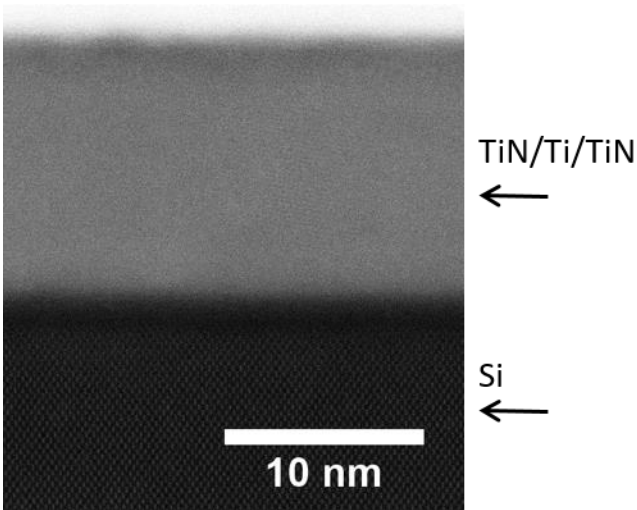


Fig. 7 (c). Higher magnification of STEM image shown in (b). Again, no contrast is evident between the Ti and TiN layers. However, a lattice image of Si atoms is resolved as shown. Additionally, the Si lattice image vanishes within a few nm of the Si/TiN interface, which is consistent with what we expect given, as described in the text, the substrate pretreatment in the sputtering system prior to TiN deposition.

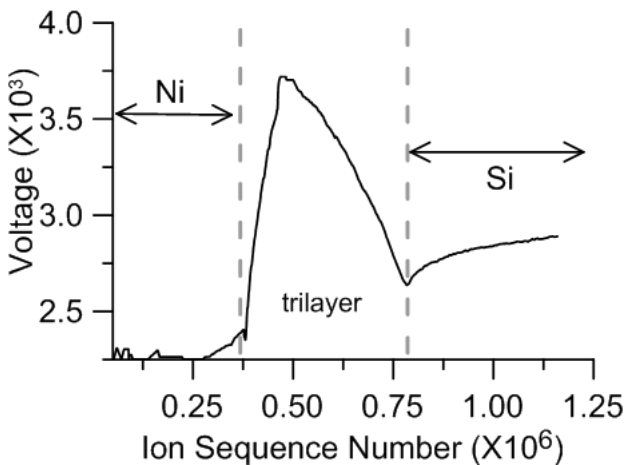


Fig. 8 (a). Variation in specimen voltage for reconstruction 7. In comparing with the case of reconstruction 2 (Fig. 2), which illustrated an example for a specimen of type 1(a), the voltage in the present case changes less abruptly as the Ti/TiN interfaces are penetrated. In particular, the relatively discontinuous voltage inflection associated with the first Ti/TiN interface noted in Fig. 2 is absent in this case.

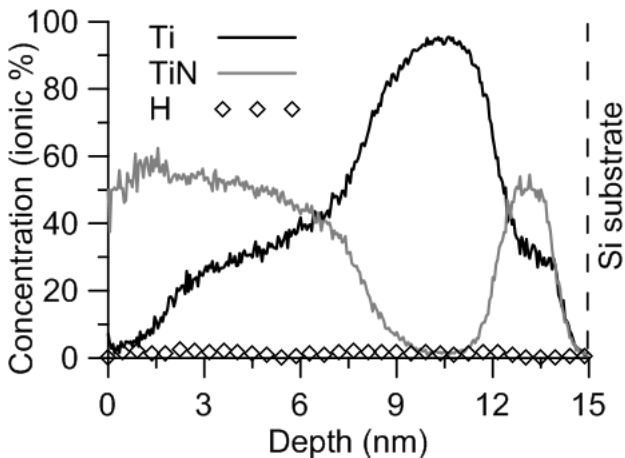


Fig. 8 (b). Axial concentration profile of Ti, TiN, and H ionic species for reconstruction 7. The result indicates a significantly reduced H concentration as compared to the case reconstruction 2 illustrated Fig. 6 (a).

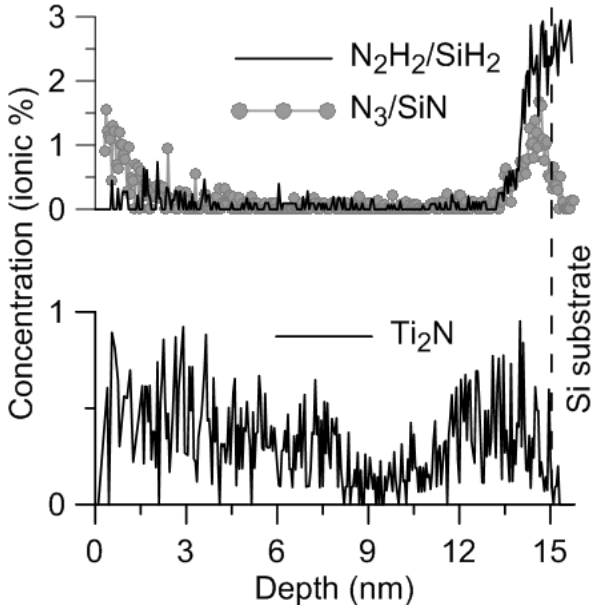


Fig. 8 (c). Both upper and lower portions of the graph were derived from reconstruction 7. Upper portion: Axial concentration profile for the ambiguous respective pairs of molecular ionic species  $N_2H_2$ ,  $SiH_2$ ; and  $N_3$ ,  $SiN$ . All may be plausibly associated with the TiN/Si interface as described in the text. Additionally,  $N_3$  may also plausibly originate from the top TiN layer to a depth of roughly 2 nm. Lower portion: Axial concentration profile of the non-superconducting  $Ti_2N$  ionic species. Compared to reconstruction 2,  $Ti_2N$  is also evident in both TiN layers but  $TiH$  is absent.

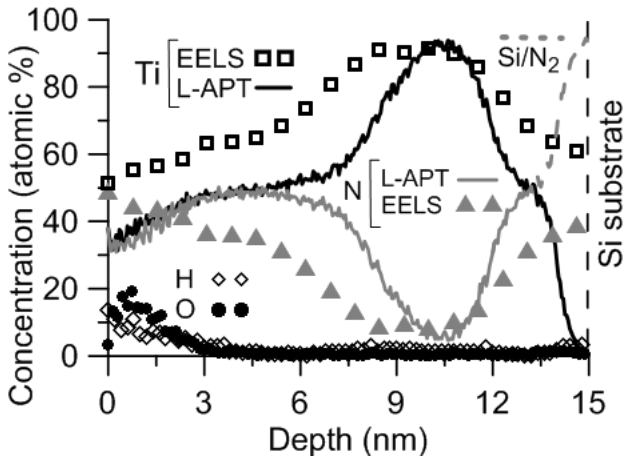


Fig. 9. Comparative axial concentration profile of Ti and N atomic species as measured by L-APT and EELS. The L-APT result is derived from reconstruction 7 and the Ti and N counts originate from both elemental and decomposed molecular ions. In contrast to the prior result for reconstruction 2 (Fig. 7 (a)), however, we also retain the minor species H and O (from both elemental and decomposed ions) in order to illustrate their occurrence within a few nm of the surface. Neither L-APT nor EELS indicate sharp interfaces between Ti and TiN layers. The ambiguous L-APT assignment between Si and N species near the TiN/Si interface is indicated.

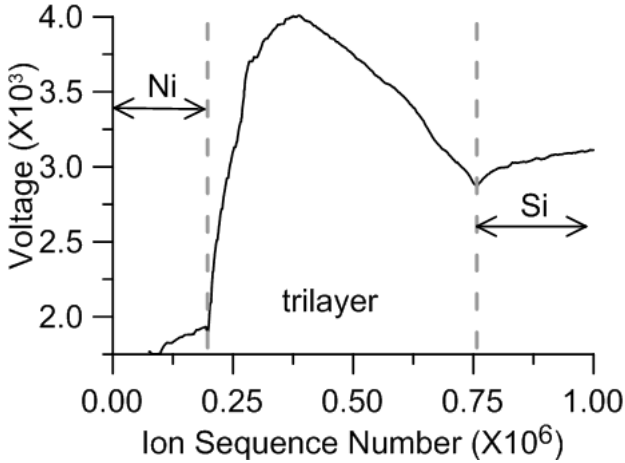


Fig. 10 (a). Variation in specimen voltage for reconstruction 11. The result is similar to that shown in Fig. 8 (a) and also lacks the strong inflection associated with the first Ti/TiN interface that was noted in Fig. 2.

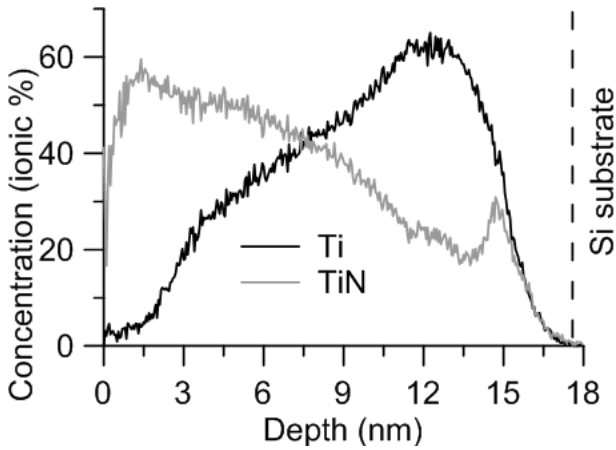


Fig. 10 (b). Axial concentration profile for ionic Ti and TiN computed from reconstruction 11. Note that in contrast to the prior examples, TiN is observed throughout the depth of the trilayer specimen.

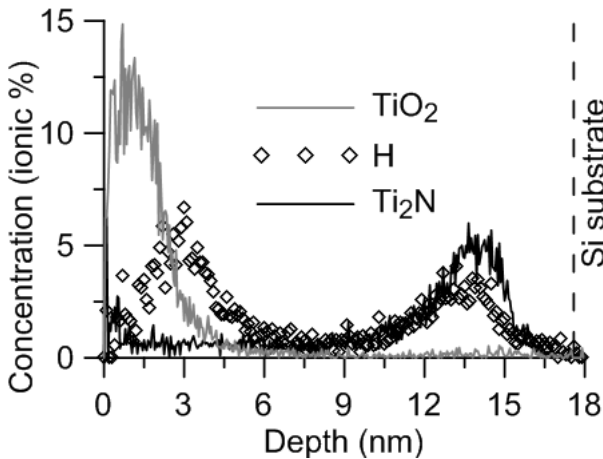


Fig. 10 (c). Axial concentration profile of ionic  $\text{TiO}_2$ ,  $\text{Ti}_2\text{N}$  and H, computed from reconstruction 11. In contrast to prior samples,  $\text{TiO}_2$  is quite evident and isolated to near the top surface of the specimen, H is primarily found at both Ti/TiN interfaces, and the non-superconducting  $\text{Ti}_2\text{N}$  phase is isolated near the first Ti/TiN interface.

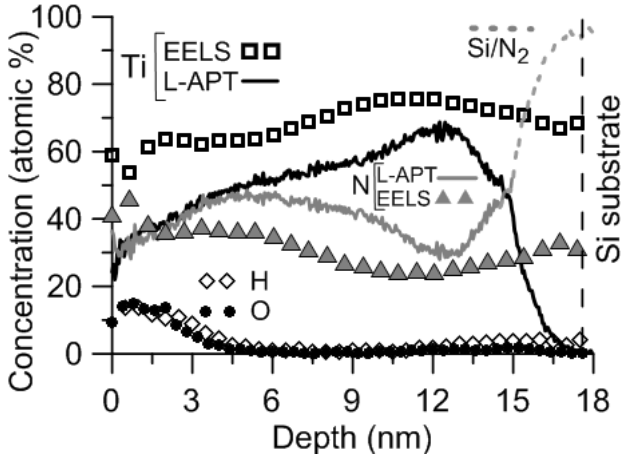


Fig. 11. Comparative axial concentration profiles of Ti and N atomic species as measured by L-APT and EELS. The L-APT result is derived from reconstruction 11 and the Ti and N counts originate from both elemental species and decomposed molecular ions. In contrast with Fig. 7 (a), the minor species H and O (from both elemental and decomposed ions) are also shown in order to illustrate their occurrence within a few nm of the surface. L-APT and EELS both illustrate less contrast between Ti and TiN layers than shown in either Figs. 7 (a) or 9. The ambiguous L-APT assignment between Si and N species near the TiN/Si interface are also indicated.

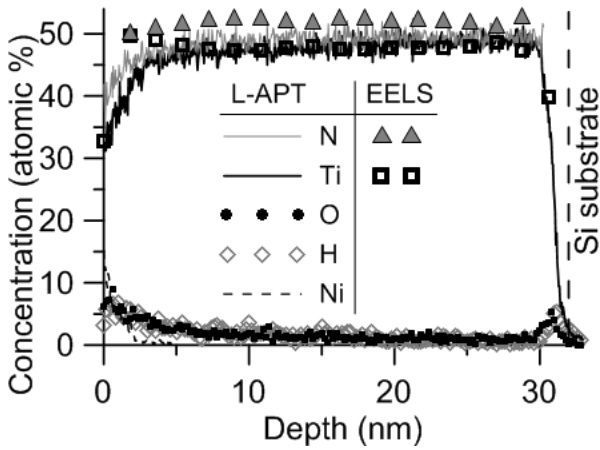


Fig. 12. Comparative axial concentration profiles of Ti and N atomic species as measured by L-APT (reconstruction 13) and EELS for TiN control sample deposited at RT. L-APT concentration profiles shown for N, Ti, O, H, and Ni are derived from both elemental and molecular ionic species. The non-superconducting  $Ti_2N$  phase (not shown) occurs roughly uniformly throughout the film at a concentration of  $\approx 0.5$  ionic %. The L-APT data has been parsed to include remnant Ni near the film surface.

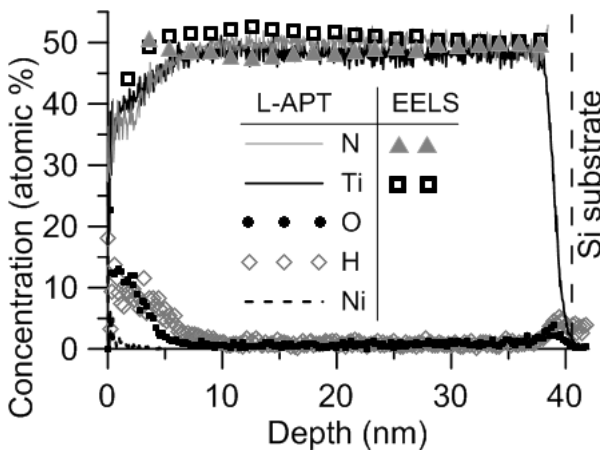


Fig. 13. Comparative axial concentration profiles of Ti and N atomic species as measured by L-APT (reconstruction 17) and EELS for the TiN control sample deposited at 500 °C. L-APT concentration profiles shown for N, Ti, O, H, and Ni are derived from both elemental and molecular ionic species. The non-superconducting  $Ti_2N$  phase (not shown) occurs at  $\approx 1$  ionic % near the surface of the film,  $\approx 0.5$  ionic % in the bulk of the layer, and  $\approx 0.7$  ionic % near the Si/film interface. The L-APT data has been parsed to include remnant Ni near the film surface.

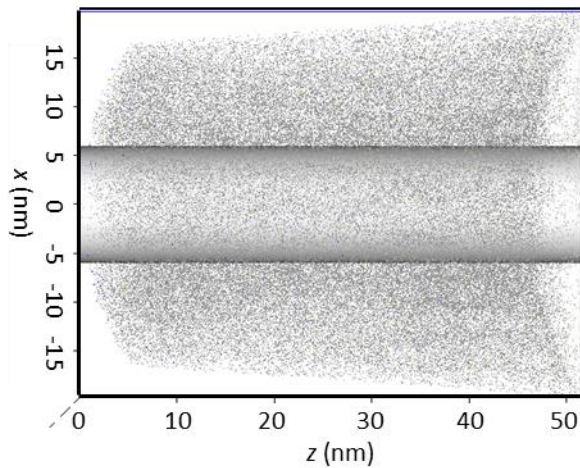


Fig. 14 (a). A two-dimensional view of reconstruction 20 for the Ti control sample deposited at RT. The coaxial placement of a separate cylindrical analysis region (12 nm in diameter) is also illustrated. A low density of detected Ti atoms was used to display the reconstruction in order to render it sufficiently transparent to allow viewing the cylinder.

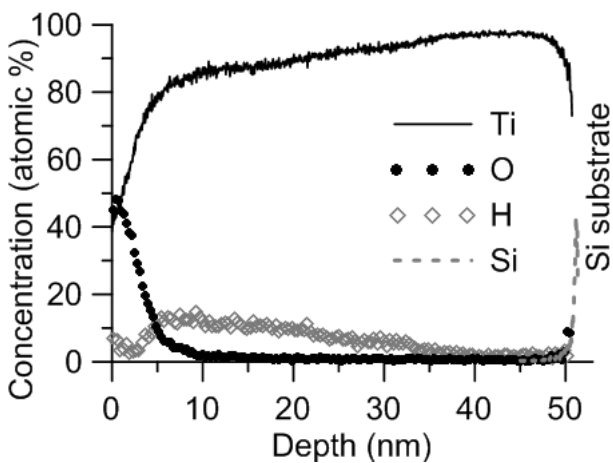


Fig. 14 (b). Axial concentration profiles for Ti, O, and H as derived from reconstruction 20 for both elemental and molecular ionic species. A portion of the Si substrate at the periphery of the reconstruction (as the film/Si interface is approached) is also detected. The data are collected from the full volume of the reconstruction as shown in (a).

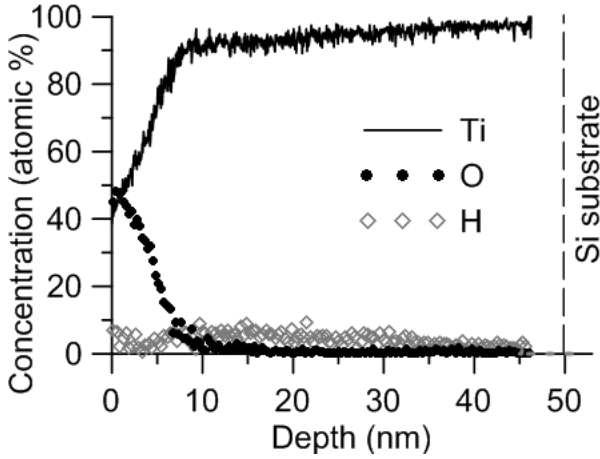


Fig. 14 (c). Similar to (b) except the analysis is confined to the cylindrical region shown in (a). The length of the analyzed region is roughly 5 nm shorter than that shown in (b) due to the curvature of the specimen tip. Si is therefore not detected within the cylindrical analysis volume.

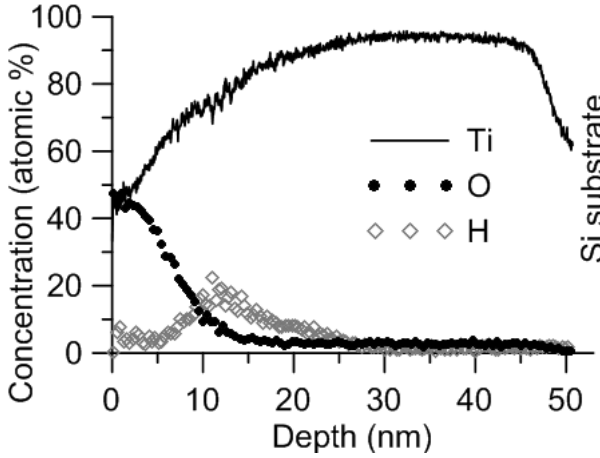


Fig. 15 (a). Reconstruction 22 results for Ti control sample deposited at 500 °C. Axial concentration profiles are shown for Ti, O, and H as derived from both elemental and molecular ionic species. The axis of the specimen tip was not perpendicular with respect to the film/Si interface therefore the Ti counts are seen to fall gradually as the depth approaches the estimated film thickness of 50 nm.

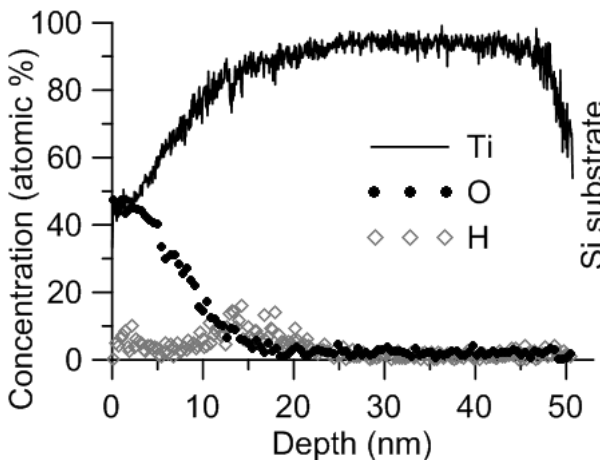


Fig. 15 (b). Similar to (a) except the analysis is confined to a coaxial cylinder 12.5 nm in diameter that extends over the depth of reconstruction 22.